High-frequency response of classical strongly coupled plasmas

Yongjun Choi,[1,*] Gautham Dharuman,[2,†] and Michael S. Murillo[2]
[1]*Institute for Cyber-Enabled Research, Michigan State University, East Lansing, Michigan 48824, USA*
[2]*Computational Mathematics, Science and Engineering, Michigan State University, East Lansing, Michigan 48824, USA*

(Received 28 January 2019; revised manuscript received 13 May 2019; published 17 July 2019)

The dynamic structure factor (DSF) of the Yukawa system is here obtained with highly converged molecular dynamics (MD) over the entire liquid phase. The data provide a rigorous test of theoretical models of ion-acoustic wave-dispersion relations, the intermediate scattering function, and the high-frequency response. We compare our MD results with seven diverse models, finding good agreement among those that enforce the three basic sum rules for dispersion properties, although one of the models has previously unreported spurious peaks. The MD simulations reveal that at intermediate frequencies ω, the high-frequency response of the DSF follows a power law, going approximately as ω^{-p}, where $p > 0$, and p shows nontrivial dependencies on the wave vector q and the plasma parameters κ and Γ. In contrast, among the seven comparison models, the predicted high-frequency response is found to be independent of $\{q, \kappa, \Gamma\}$. This high-frequency power suggests a useful fitting form. In addition, these results expose limitations of several models and, moreover, suggest that some approaches are difficult or impossible to extend because of the lack of finite moments. We also find the double-plasmon resonance peak in our MD simulations that none of the theoretical models predicts.

DOI: 10.1103/PhysRevE.100.013206

I. INTRODUCTION

The dynamic structure factor (DSF) plays a central role in our understanding of strongly coupled plasmas because it provides a clean description of the equilibrium dynamics of correlations that occur in white dwarfs [1], giant planets [2], dusty plasmas [3], ultracold plasmas [4], and dense plasmas [5]. In particular, the DSF contains dynamical information needed to properly describe and model collective modes and transport [6–9], while also providing information on stopping power [10,11], neutron scattering [12], x-ray Thomson scattering (XRTS) [13], and microfields [14]. Increasingly accurate DSF models improve our understanding of dynamical correlations and provide an additional rationale for the use of XRTS as an experimental diagnostic, as well. A survey of extant DSF models reveals a wide diversity of approaches, including early work on memory functions by Hansen and coworkers [15,16], the dynamic local field correction (DLFC) models of Tanaka and Ichimaru [17] and Hong and Kim [18], the sum-rule approaches of Adamjan *et al.* and others [19–23], Mermin's relaxation-time approximation [24], and Murillo's modified Navier-Stokes equation [6], to name only a few.

A comprehensive comparison across diverse models and detailed molecular dynamics (MD) validation are needed to exclude less accurate models from consideration and to suggest research directions with the largest potential impacts on applications. Several reports have compared theoretical models with MD data, but, to our knowledge, all such studies used a specific set of plasma parameters or very limited plasma regimes and examined at most three models [25–28]. Here, we compare seven models with new, highly accurate MD simulations across the entire liquid phase. We find that for some quantities, many models are in agreement, but for other properties, none of the models are accurate.

Most models of the DSF are formulated with pair potentials to avoid dependencies on spatial correlations that are of higher order than the order of the radial distribution function $g(r)$; therefore, we similarly limited our study to systems described by pair potentials, and we also considered only three-dimensional plasmas. We chose the Yukawa potential both because it is the most widely used pair potential and because it very accurately describes ultracold plasmas [29], dusty plasmas [30], dense plasmas [31,32], and white dwarfs [1]. The Yukawa potential is

$$\phi(r) = \frac{Q^2}{r}\exp(-r/\lambda_s), \tag{1}$$

where Q is the effective ion charge and λ_s is an appropriate screening length associated with free-electron polarization. In equilibrium at temperature T, the Yukawa system is described through two dimensionless parameters, the screening parameter $\kappa = a/\lambda_s$ and the coupling parameter $\Gamma = Q^2/aT$, where $a = (3/4\pi n)^{1/3}$ is the ion-sphere radius in terms of the ionic density n; the one-component plasma (OCP) model is the $\kappa = 0$ case. For this study, we examined a wide range of (κ, Γ) pairs, with $\kappa = 0$–3 and $\Gamma = 10$–1510; this parameter space covers long- and short-range interactions, as well as moderate to strong coupling. Because the plasmas we model are in equilibrium, it is not necessary to include dynamical corrections [33] to the Yukawa potential, as the ions always move more slowly than the electron thermal velocity. In some scenarios, modifications of the Yukawa potential may be beneficial, for example, when considering wake potentials

*Corresponding author: choiyj@msu.edu
†Present address: Lawrence Livermore National Laboratory, Livermore, CA 94550, USA.

[34] in dusty plasmas near sheath regions; however, we do not include such field-specific corrections to keep our results as general as possible.

The rest of this paper is organized as follows. In Sec. II, several theoretical models, together with our methods, are described. In Sec. III, we discuss our numerical simulations in detail. Simulation parameters that we obtained by testing a variety of simulation conditions are given in Sec. IV. In Sec. V, we compare the theoretical models with our numerical simulations, and finally, we offer our conclusions in Sec. VI.

II. MODELS AND METHODS

MD plays a key role in establishing our confidence in models for the DSF [16,35,36]. MD simulations have been performed here using standard methods (e.g., velocity-Verlet integration), with the addition of an efficient generalization of the particle-particle particle-mesh (PPPM) method to Yukawa interactions [36]. We carefully examined convergence issues related to particle number, time step, and number of time steps, using primarily $N = 10\,000$, $\Delta t = 0.01$, and $N_{\rm steps} = 80\,000$. The Fourier-transformed density $n(q,t)$ was extracted from simulation data to form the intermediate scattering function (ISF) $F(q,t)$ and its Fourier transform, the DSF $S(q,\omega)$. Wave vectors $\mathbf{q} = 2\pi\hat{l}/L$, where $\hat{l}$ is a vector formed from integers, were chosen based on periodicity constraints set by the simulation cell size, which is indirectly determined by the density and number of particles through $L = (N/n)^{1/3}$. Because the plasmas we consider are isotropic, we computed quantities in several directions and averaged to improve the statistics. We use reduced units in which the wave number q is in units of a^{-1}, the frequency ω is in units of ω_p, with the ion plasma frequency $\omega_p = (4\pi nQ^2/m)^{1/2}$ for ionic mass m, and the time t is in units of ω_p^{-1}. With these quantities, the DSF and its frequency moments are defined as

$$S(q,\omega) = \int_{-\infty}^{\infty} dt\, F(q,t) e^{i\omega t}, \tag{2}$$

$$S_l(q) = \int_{-\infty}^{\infty} \frac{d\omega}{2\pi} \omega^l S(q,\omega),\ l = 0, 2, 4 \ldots. \tag{3}$$

The odd-order moments vanish because of the symmetry of the DSF. If several of the $S_l(q)$ are known, models of $S(q,\omega)$ can be constrained; with only $g(r)$ as an input, three frequency moments can be constructed that constrain the area, mean, and variance of $S(q,\omega)$. For the Yukawa model, these constraints yield the sum rules

$$\begin{aligned}
S_0(q) &= S(q),\\
S_2(q) &= q^2/3\Gamma,\\
S_4(q) &= S_2(q)\left[\frac{q^2}{q^2+\kappa^2} + \frac{q^2}{\Gamma} + I(q)\right],\\
I(q) &= \frac{1}{12\pi}\int_0^{\infty} f(q,\tilde{q})(1 - S(q))\tilde{q}^2 d\tilde{q},\\
f(q,\tilde{q}) &= \frac{2(3q^2 - \kappa^2 - \tilde{q}^2)}{q^2} + \frac{(q^2 - \kappa^2 - \tilde{q}^2)^2}{2q^3\tilde{q}}\\
&\quad \times \ln\left(\frac{\kappa^2 + (q+\tilde{q})^2}{\kappa^2 + (q-\tilde{q})^2}\right) - \frac{8\tilde{q}^2}{3(\kappa^2 + \tilde{q}^2)},
\end{aligned} \tag{4}$$

where $S(q)$ is the static structure factor and $I(q)$ is the static local field correction in the high-frequency limit.

We now describe seven theoretical approaches that we will compare with our MD simulations. We begin with Mermin (M) [24], who proposed a relaxation-time approximation to include collisions in the susceptibility $\chi(q,\omega)$. The M model satisfies only $S_2(q) = q^2/3\Gamma$, the "f-sum rule," and it can be written as

$$\chi(q,\omega) = \left(1 - \frac{i\omega}{\nu}\right)\frac{\chi_{\rm RPA}(q,\omega+i\nu)\chi_{\rm RPA}(q,0)}{\chi_{\rm RPA}(q,\omega+i\nu) - (i\omega/\nu)\chi_{\rm RPA}(q,0)}, \tag{5}$$

where ν is a collision frequency, the only input, and $\chi_{\rm RPA}$ is the random-phase approximation (RPA) susceptibility. The DSF is obtained through the fluctuation-dissipation theorem,

$$S(q,\omega) = -\frac{2T}{n\omega}\chi''(q,\omega), \tag{6}$$

where $\chi''(q,\omega)$ is the imaginary part of $\chi(q,\omega)$. The M model contains no information about correlations beyond the mean field. The appeal of the M model is that it includes collisions beyond the mean field without violating particle conservation; however, inclusion of other conservation laws reveals [10,37] that particle conservation alone may *decrease* accuracy. Here, because of our interest in the functional form of the model, we fit M to the MD data to obtain the "best" value for ν.

Next, we review three models that exploit the frequency-moment sum rules. Because the models exploit the same three sum rules, they yield very similar predictions. The promise of such models is that, in principle, more sum rules can be included to systematically improve accuracy. However, this approach fails when no moments exist; such situations are discussed below. Staying within a susceptibility model, the dynamic local field correction $G(q,\omega)$ can be used to model both collisions and correlations through

$$\chi(q,\omega) = \frac{\chi_0(q,\omega)}{1 - v(q)[1 - G(q,\omega)]\chi_0(q,\omega)}, \tag{7}$$

where $\chi_0(q,\omega)$ is the susceptibility of the ideal gas, and $v(q)$ is the Fourier transform of the pair potential. The DLFC is defined such that when $G(q,\omega) = 0$, one obtains the mean-field (RPA) result. Simple models for the DLFC can be obtained by replacing it with the static local field correction $G(q)$ or with its high-frequency limit, $I(q) \equiv G(q,\omega = \infty)$. However, it is well known that these simpler models are accurate only under limited conditions [38–40].

Tanaka and Ichimaru (TI) developed a model that includes high- and low-frequency limits using a viscoelastic formalism [17], writing

$$G(q,\omega) = \frac{G(q) - i\omega\tau_M(q)I(q)}{1 - i\omega\tau_M(q)}, \tag{8}$$

where $\tau_M(q)$ is the viscoelastic relaxation time. This model satisfies the three moment relations, which are not sufficiently constraining to obtain $\tau_M(q)$. TI suggest either a Gaussian or Lorentzian form for $\tau_M(q)$; here, we fit to the MD data for each q, and this approach allows us to examine the TI ansatz for the "best" possible $\tau_M(q)$.

Hong and Kim (HK) proposed a related model [18] that also enforces the three moments. They adopted the

TABLE I. Summary of the theoretical models. M, Mermin's collision approach; TI, Tanaka and Ichimaru's DLFC model; HK, Hong and Kim's DLFC model; A, Arkhipov *et al.*'s momentum approach; MNS, Murillo's modified Navier-Stokes model; G, Gaussian memory function; and E, exponential memory function.

Model	Source	Key physics	Focus	Moments	Asymptotic power of ω
M	[24]	Collisions	$\chi(q,\omega)$	2	-4
TI	[17]	Viscoelastic formalism	$G(q,\omega)$	0, 2, 4	-6
HK	[18]	Recurrence relation method	$G(q,\omega)$	0, 2, 4	Exponential decay
A	[23]	Nevanlinna	$S(q,\omega)$	0, 2, 4	-6
MNS	[6]	Structure and viscosity	$S(q,\omega)$	0, 2	-4
G	[15,16]	Memory function	$S(q,\omega)$	0, 2, 4	Exponential decay
E	[41,42]	Memory function	$S(q,\omega)$	0, 2, 4	-6

first-, second-, and third-order approximation parameters to obtain the DLFC. The first-order approximation is to replace $G(q,\omega)$ with $G(q)$. The second-order approximation is to set $\eta_3 = 0$. The third-order approximation is

$$G(q,\omega) = G(q) - \frac{q^2+\kappa^2}{3\Gamma}\frac{[\eta_2 - \eta_3 R(x)]Q(x)}{1+\eta_3 R(x)}, \tag{9}$$

where $x = \sqrt{\frac{3\Gamma}{2}}\frac{\omega}{q}$, $Q(x) = 1/Z(x) + 2x^2 - 1$, $R(x) = 1 - \frac{1}{2}Q(x)$, $Z(x) = [1 - 2xD(x)] + i\sqrt{\pi}x\,\exp(-x^2)$, $D(x)$ is the Dawson function, $\eta_2 = (3\Gamma)/[2(q^2+\kappa^2)][G(q) - I(q)]$, and η_3 involves the sixth moment of the DSF, $S_6(q)$. Because theoretical calculation of $S_6(q)$ requires correlation information beyond $g(r)$, HK treated η_3 as a fitting parameter. Note that, because $\chi_0(q,\omega)$ appears in the numerator of the M, TI, and HK models, there is an exponential decay in the weakly coupled limit, allowing an arbitrary number of moments to be used; this property is lost, however, when collisions are included, as we will see below.

Adamjan *et al.* developed another sum-rule approach, based on the Nevanlinna formula of the classical theory of moments method, to construct the OCP DSF [19], and this approach has been explored for hydrogen-like two-component plasmas [20–22]. Recently, Arkhipov *et al.* (A) expanded this sum-rule approach to Yukawa OCPs (YOCPs) [23], finding

$$\frac{S(q,\omega)}{S(q)} = \frac{\sqrt{2}\omega_1^3\omega_2^2(\omega_2^2-\omega_1^2)}{2\omega^2\omega_1^2(\omega^2-\omega_2^2)^2 + \omega_2^4(\omega^2-\omega_1^2)^2}, \tag{10}$$

where $\omega_1^2(q) = S_2(q)/S(q)$, and $\omega_2^2(q) = S_4(q)/S_2(q)$. While this form satisfies the same sum rules as the M, TI, and HK models, it does not contain the RPA or ideal-gas limits.

Murillo constructed a modified Navier-Stokes equation (MNS) model [6] that yields

$$S(q,\omega) = \frac{8\sqrt{3}\omega_E}{9\Gamma}\frac{q^4\widetilde{\eta}}{\left(\omega^2 - \frac{q^2}{3\Gamma S(q)}\right)^2 + \left(\frac{4\sqrt{3}\omega_E}{3}q^2\omega\widetilde{\eta}\right)^2}, \tag{11}$$

where $\widetilde{\eta}$ is the dimensionless viscosity and ω_E is the Einstein frequency in units of ω_p, where $\omega_E = \frac{\kappa^2}{3}\int_0^\infty r\exp(-\kappa r)g(r)dr$ for the YOCP and $\omega_E = \frac{1}{3}$ for the OCP. While this model has the correct hydrodynamic limit and includes correlations and collisional damping, it does not describe the ideal-gas limit; it also does not satisfy the high-frequency sum rule [1].

Finally, the DSF can also be obtained from generalized hydrodynamics [15,16,41] by modeling the memory function, giving

$$\frac{S(q,\omega)}{S(q)} = \frac{2\omega_1^2 q^2\phi'_{MF}(q,\omega)}{\left[\omega^2 - \omega_1^2 - \omega q^2\phi''_{MF}(q,\omega)\right]^2 + [\omega q^2\phi'_{MF}(q,\omega)]^2}, \tag{12}$$

where $\phi'_{MF}(q,\omega)$ and $\phi''_{MF}(q,\omega)$ are the real and imaginary parts of the Laplace transform of the memory function $\phi_{MF}(q,t)$, respectively. For $\phi_{MF}(q,t)$, either the Gaussian (G) or exponential-function (E) model is usually used. Note the resemblance to the MNS model given in Eq. (11).

Table I summarizes properties of the seven models discussed above, including the moments that each satisfies and the predicted form of the high-frequency tail. The seven models yield three—significantly different—predictions of the form of the tail: exponential decay and two power-law (ω^{-p}, $p = 4$ and $p = 6$) forms of decay. Even though the TI and HK models use the DLFC, they show very different asymptotic powers, because $G''(q,\omega)$, the imaginary part of the DLFC, is proportional to ω^{-1} in the TI model, while it decays exponentially in the HK model at high frequencies.

If the DSF is available, we can obtain the susceptibility via Eq. (6) and the Kramers-Kronig relations

$$\begin{aligned}\chi'(q,\omega) &= \mathcal{P}\int_{-\infty}^{\infty}\frac{d\tilde{\omega}}{\pi}\frac{\chi''(q,\tilde{\omega})}{\tilde{\omega}-\omega},\\ \chi''(q,\omega) &= -\mathcal{P}\int_{-\infty}^{\infty}\frac{d\tilde{\omega}}{\pi}\frac{\chi'(q,\tilde{\omega})}{\tilde{\omega}-\omega}.\end{aligned} \tag{13}$$

However, in reality, it is very difficult to obtain the susceptibility via the Kramers-Kronig relations using the DSF from the MD data because of noise. For the MD results, we can obtain the susceptibility via the Laplace transform of $F(q,t)$,

$$\begin{aligned}g(q,\omega) &\equiv \int_0^\infty dt F(q,t)e^{i\omega t}\\ &= \int_{-\infty}^{\infty} dt F(q,t)H(t)e^{i\omega t}\\ &= g'(q,\omega) + ig''(q,\omega),\end{aligned} \tag{14}$$

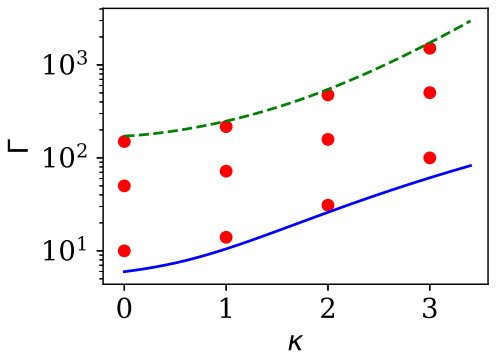

FIG. 1. The (κ, Γ) pairs for which the DSF was computed using MD simulations. The solid blue and dashed green lines are the lower and upper limits of the liquid regime, respectively, and red dots indicate data points used in this study. Note that the points were chosen to span the strongly coupled liquid regime, and they roughly follow contours of constant effective coupling.

where $H(t)$ is the Heaviside step function, and

$$g'(q,\omega) = \frac{1}{2}S(q,\omega),$$
$$g''(q,\omega) = \frac{1}{2\pi}\int_{-\infty}^{\infty} d\tilde{\omega}\frac{S(q,\tilde{\omega})}{(\omega-\tilde{\omega})}. \quad (15)$$

From Eqs. (6), (15), and the Kramers-Kronig relations in (13), we can express $g(q,\omega)$ as

$$g'(q,\omega) = -\frac{T}{n\omega}\chi''(q,\omega),$$
$$g''(q,\omega) = \frac{1}{\omega}S(q) + \frac{T}{n\omega}\chi'(q,\omega). \quad (16)$$

III. SIMULATIONS

We used a range of (κ, Γ) pairs across coupling regimes: $(\kappa = 0,\ \Gamma = 10, 50, 150)$, $(\kappa = 1,\ \Gamma = 14, 72, 217)$, $(\kappa = 2,\ \Gamma = 31, 158, 476)$, and $(\kappa = 3,\ \Gamma = 100, 503, 1510)$. Figure 1 shows the (κ, Γ) pairs, together with the lower and upper boundaries of the liquid regime [6]. The (κ, Γ) pairs were chosen to approximately follow contours of constant effective coupling.

Our MD simulations employed standard methods, including velocity-Verlet integration using a PPPM Yukawa force algorithm [36]. For all results presented, we ran 20 simulations of 10^4 particles, giving the required convergence at long wavelengths. For the PPPM algorithm, the Ewald parameter was 0.46 (distances are in units of a^{-1}). For the particle-particle portion of the calculation, the cutoff radius was 7.8; for the particle-mesh portion, the grid dimensions were $64 \times 64 \times 64$, and B-splines were of order 6. These parameters correspond to an error of $\approx 10^{-6}$ (e^2/a^2) in the computed forces. The simulations were carried out with the Berendsen thermostat for the first 10 000 steps to reach the equilibrium state. For the next 80 000 steps, we turned off the thermostat and collected data. For a whole simulation time span, the time step Δt was chosen to be 0.01 (times are in units of ω_p^{-1}) to ensure the required energy conservation. The time step was dictated by the lowest Γ at $\kappa = 0$ because hard collisions

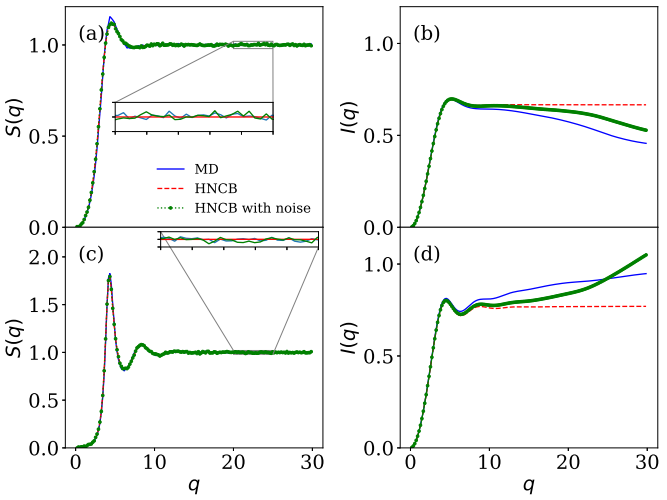

FIG. 2. $S(q)$ and $I(q)$ calculated from the MD and HNCB results. $S(q)$ is shown in the left panels, and $I(q)$ is shown in the right panels. The MD results are shown with solid lines, the HNCB results are shown with dashed lines, and dotted lines indicate the HNCB results with Gaussian random noise added to mimic the MD simulations. Panels (a) and (c) show that the static structure factor from the MD and the HNCB results are in close agreement, and the addition of noise results in even better agreement. Panels (b) and (d) show that $I(q)$ obtained from the MD simulations is very different from $I(q)$ from the HNCB results at large q. Adding noise to the HNCB results yields an $I(q)$ similar to the MD results at large q, revealing the large sensitivity to statistical averaging; moreover, these results show that the addition of noise can either reduce or increase $I(q)$.

are more prominent at smaller Γ for a given κ. The quality of energy conservation was quantified using an error metric defined as $\Delta E(\%) = \frac{100}{M}\sum_{j=1}^{M}|\frac{E(t_j)}{E(0)} - 1|(\%)$, which is the percentage error accumulated in time with respect to the initial energy of the system after equilibration. Energy conservation was excellent for all of the simulations, with $\Delta E \sim 10^{-6}\%$.

To evaluate the theoretical models, it is necessary to estimate the static structure factor $S(q)$; in general, we attempted to obtain $S(q)$ directly from a frequency integration of $S(q,\omega)$, which was obtained from the Fourier-transformed density [36]. However, when q is very small, the DSF has a very narrow peak, and therefore, there is a possibility that $S(q)$ obtained from MD is not accurate. To compensate for this inaccuracy, we also employed the hypernetted-chain approximation with a bridge function (HNCB) [43] to obtain $S(q)$ at small q.

Most theoretical models in this study require three sum rules, $S(q)$, $S_2(q)$, and $S_4(q)$. $S(q)$ can be calculated easily from the DSF, and $S_2(q) = q^2/3\Gamma$. $S_4(q)$ is a function of $I(q)$ and $S(q)$. However, the behavior of $I(q)$ is rarely described. Here, we present $S(q)$ and $I(q)$ from MD simulations; our results are shown in Fig. 2. In addition, we used the HNCB [43] to obtain $S(q)$, and we compare the MD and HNCB results. In Fig. 2, our MD simulations are shown with solid blue lines, our HNCB results are shown with dashed red lines, and the HNCB results, with Gaussian random noise added to mimic the MD simulations, are shown with dotted green lines. Figures 2(a) and 2(c) show that the MD and HNCB results yield very similar static structure factors, and the addition of

noise results in even closer agreement. Figures 2(b) and 2(d) show $I(q)$ obtained from $S(q)$. We can see that the HNCB and MD approaches give very different $I(q)$ for large q. However, the addition of noise to the HNCB results moves them much closer to the MD simulations at large q. Moreover, we see that adding noise to the HNCB results may either reduce or increase $I(q)$; this suggests that a very large number of particles are required to obtain accurate $I(q)$ at large wave numbers.

IV. MD CONVERGENCE TESTS

To obtain accurate MD simulation results, it is important to determine reasonable simulation parameters, including the number of particles (N), the time step (dt), and the timespan ($T_s = N_{\text{step}} \times dt$). In this section, we present the results of convergence tests for our MD simulations under various conditions. All simulations were performed with $\kappa = 3$ and $\Gamma = 1500$, and all results are averaged over 20 runs. The frequency bin size $d\omega$ is $2\pi/T$.

Figure 3 shows the DSFs for three different numbers of particles for $q = 1.86$ and $q = 3.40$. Because we use periodic boundary conditions (PBCs), direct calculation of the DSFs when $q = 1.86$ and $q = 3.40$ is not possible for $N = 5000$ and $N = 10000$; therefore, the DSFs for each wave number when $N = 5000$ and $N = 10\,000$ were obtained through a linear interpolation of DSFs at the nearest available wave numbers. These interpolated DSFs are compared with the DSFs for $N = 2000$. The solid ($N = 10\,000$), dashed ($N = 5000$), and dotted ($N = 2000$) lines in Fig. 3 indicate smoothed results obtained using a Savitzky-Golay filter [44], with the window length set to 13 and the polynomial order set to 3. Figure 3 shows that the simulations for all three numbers of particles are in good agreement; small differences in the results for different numbers of particles may be due to statistical noise and fluctuations resulting from small $d\omega$. These results show that 10 000 particles are sufficient to describe the dynamic characteristics of the Yukawa potential.

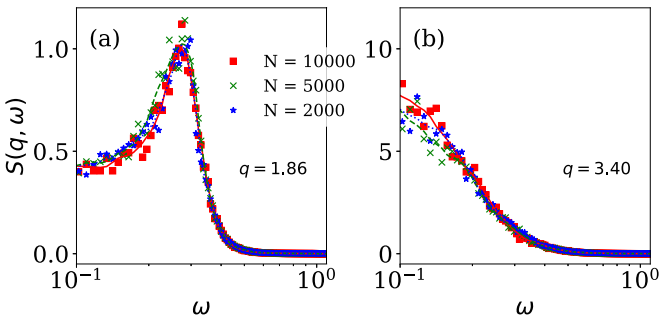

FIG. 3. The DSF for three different numbers of particles: $N = 2000, 5000$, and $10\,000$. All simulations were performed with the plasma parameters ($\kappa = 3$, $\Gamma = 1500$), and the wave number was set to either $q = 1.86$ (left panel) or $q = 3.40$ (right panel). The results of all three simulations are in good agreement, indicating convergence of the simulations at a modest particle number. The raw data are shown as individual points in both panels. The solid ($N = 10\,000$), dashed ($N = 5000$), and dotted ($N = 2000$) lines are smoothed using a Savitzky-Golay filter.

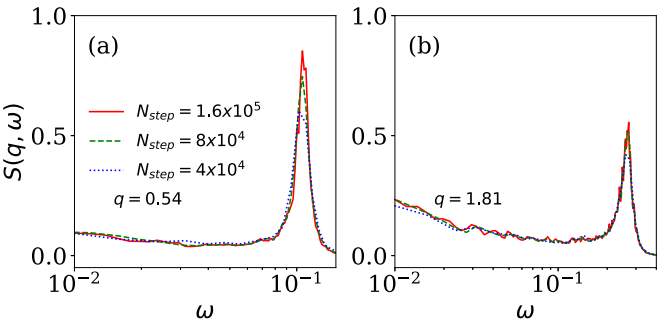

FIG. 4. The DSF for three different numbers of time steps. All simulations were performed with plasma parameters ($\kappa = 3$, $\Gamma = 1500$), and the wave number was set to either $q = 0.54$ (left panel) or $q = 1.81$ (right panel). The results of all three sets of simulations exhibit very close agreement. These results reveal the importance of long runs for capturing the correct peak value of the DSF.

Figure 4 shows the DSF for three different numbers of time steps. We chose $N_{\text{step}} = 40\,000$, $80\,000$, and $1\,60\,000$. The time step dt and the number of particles were fixed for all three simulations, with $dt = 0.01$ and $N = 10\,000$. Small differences in the DSF can be observed for the different numbers of time steps primarily near the peaks, which occur at $\omega \sim 0.1$ for $q = 0.54$ and at $\omega \sim 0.27$ for $q = 1.81$. These differences occur because $d\omega$ is determined by N_{step} such that $d\omega = 2\pi/(N_{\text{step}}dt)$. Away from this peak region, the results for $N_{\text{step}} = 80\,000$ and $N_{\text{step}} = 1\,60\,000$ are in very good agreement. Because determining the precise peak amplitude of the DSF is beyond the scope of this work, we chose $N_{\text{step}} = 80\,000$ for simulations, as the DSF converges sufficiently for the purposes of this study with this value of N.

Figure 5 shows the DSF calculated using three time steps ($dt = 0.01$, 0.02, and 0.04) with the system simulated for a fixed time span $T_s = 800$. The number of particles was chosen to be $10\,000$ for all simulations. We can see that all DSFs are in very close agreement. Thus, we chose $dt = 0.01$ for simulations in this study. Based on these tests, we conclude that $N = 10\,000$, $N_{\text{step}} = 80\,000$, and $dt = 0.01$ yield accurate results.

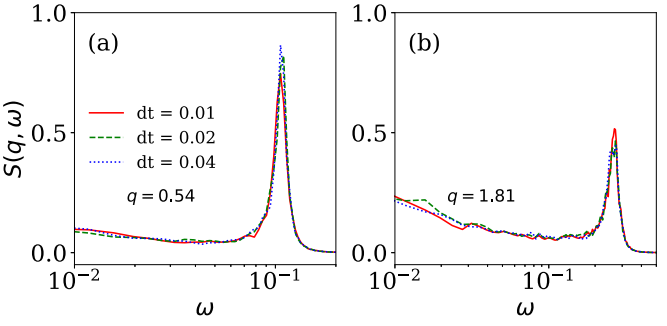

FIG. 5. The DSF for three different choices of the time step. All simulations were performed with the plasma parameters ($\kappa = 3$, $\Gamma = 1500$), and the wave number was set to either $q = 0.54$ (left panel) or $q = 1.81$ (right panel). The DSFs for all cases are in very close agreement.

V. RESULTS

As described above, we ran 20 MD simulations of $N = 10^4$ particles, with $N_{\text{step}} = 80\,000$ and $dt = 0.01$, for each (κ, Γ) pair studied across the liquid regime, as shown in Fig. 1. From these results, we calculated the DSF, $S(q, \omega)$, across the liquid regime for values of q ranging from less than 0.5 to nearly 30 and ω ranging from 10^{-2} to 10^2. Dispersion relations for given (κ, Γ) pairs were found by determining, across a range of values of q, the value of ω at which the peak DSF value occurred for a given value of q. The intermediate scattering function was also calculated from the DSF results for given (κ, Γ) pairs. These DSF, dispersion relation, and intermediate scattering function results, calculated from our MD data, were then compared with DSFs, dispersion relations, and scattering functions calculated using the seven theoretical models examined in this study.

In Subsec. V A, we compare our MD results with the theoretical models for a range of parameter values that cover the entire Yukawa liquid regime. In Subsec. V B, we offer an empirical fitting form for the DSF that captures many of the new features we have explored, and we show that this fit is in good agreement with our MD results. Finally, in Subsec. V C, we examine the double-plasmon resonance peak that appears in the MD DSF, although none of the theoretical models predict this peak.

A. Comparison of theoretical models and the MD results

In this subsection, we compare our MD results with results calculated using the seven theoretical models discussed in Sec. II. First, we examine the dispersion relation for two (κ, Γ) pairs that represent extreme limits of the effective coupling and screening. Next, we compare the DSF calculated from our MD data with those from the theoretical models. We then investigate the predicted high-frequency tail of the DSF. Finally, we compare, for a fixed value of q, the intermediate scattering function $F(q, t)$ obtained from the DSF calculated from the MD data with those calculated using the theoretical models.

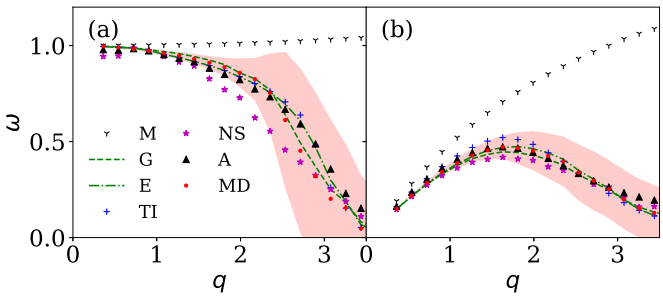

FIG. 6. Dispersion relations obtained from the theoretical models and the MD data. The plasma parameters are $(\kappa = 0, \Gamma = 150)$ in panel (a) and $(\kappa = 2, \Gamma = 31)$ in panel (b). The red band reflects damping and corresponds to the full-width-half-maximum of the MD results. The failure of the M model reflects the importance of including a $g(r)$ dependency; similarly, the lower frequencies in the MNS model reflect the lack of the high-frequency sum rule in that model. Results for the ion-acoustic wave in panel (b) show that all models except the M model predict the MD results well.

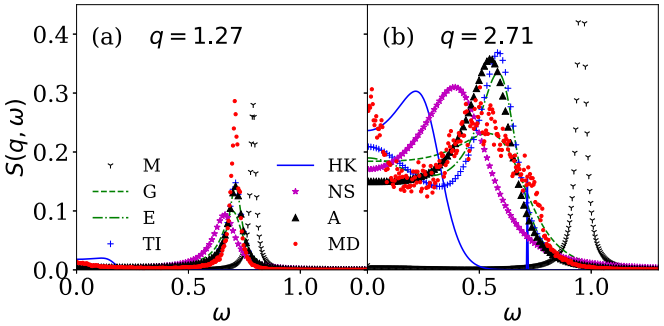

FIG. 7. The DSF $S(q, \omega)$ obtained from the theoretical models and the MD data. The plasma parameters are $(\kappa = 1, \Gamma = 217)$, and the wave numbers are either $q = 1.27$ (left panel) or $q = 2.71$ (right panel). The HK and Mermin models fail to predict the MD results. In particular, the HK model predicts two peaks, which suggests that their third-order approximations may not converge fast enough.

Dispersion relations obtained using MD are compared with those predicted by the theoretical models in Fig. 6; the dispersion relations for $(\kappa = 0, \Gamma = 150)$, corresponding to a plasma oscillation, and for $(\kappa = 2, \Gamma = 31)$, corresponding to an ion-acoustic wave, are shown. The peak of the DSF arises from the collective plasma oscillations, and its location is the plasmon frequency [26,28,45]; plasmon damping is characterized by the width of the peak (full-width-half-maximum of MD) and is shown as a light pink band. We do not include the HK model, which yielded poor predictions, in Fig. 6 for reasons that will be explained below. The M model fails to predict the dispersion relation because the collision frequency ν, treated here as a constant for a given wave number q, is independent of structural information contained in $S(q)$. The MNS model predicts a slightly lower peak frequency than the MD simulations because of its neglect of elastic physics [1]. (The viscosity was obtained from a best fit to the MD data to remove any errors arising from an inaccurate viscosity input; thus, the error shown is indicative of a poor functional form.) In general, the other four models are indistinguishable, with the exception of A, for which the results are slightly higher than the MD results for the ion-acoustic wave.

Next, in Fig. 7, we compare the full DSF, the intermediate screening and high coupling case $(\kappa = 1, \Gamma = 217)$, and two wave numbers, $q = 1.27$ and $q = 2.71$. Even though we calculate the DSF up to $q = 30$, we focus on the DSF at low wave numbers, $q \lesssim 5$, because our main interest is collective modes. This figure reveals that, while the location of the peak is accurate (Fig. 6), damping is somewhat poorly predicted by all of the models. As mentioned above, serious problems were found with the HK model. The HK model [18] satisfies the same three sum rules as the three other models discussed here and should thus yield results similar to those of the other sum-rule-based models; however, the HK model predicts *two* peaks, thereby shifting the main peak to lower frequencies to compensate for spectral weight in the higher-frequency peak. To our knowledge, this behavior of the HK model has not been seen before; however, a careful examination of their results [18] reveals an incipient shoulder on the high-frequency side, which we find bifurcates into a secondary peak at q values larger than those authors present. While we do not know the

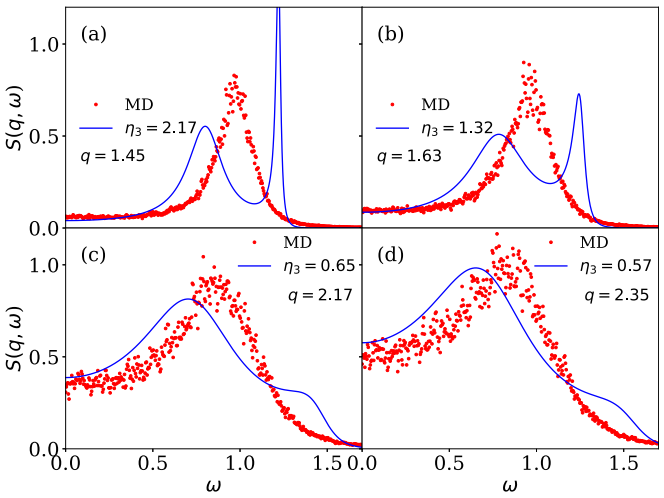

FIG. 8. The DSF obtained from the HK model. The plasma parameters are ($\kappa = 0$, $\Gamma = 150$), and the wave numbers are $q = 1.45, 1.63, 2.17, 2.35$ in panels (a) through (d), respectively. The parameter η_3 was obtained from the MD results using the least squares fitting method. The HK model shows two peaks when the wave number is small; as the wave number increases, the second peak (on the right) weakens, while the left peak dominates the spectrum and yields a more reasonable result.

source of this spurious behavior, we do not recommend the HK model without further analysis.

Figure 8 shows the DSF obtained from HK for ($\kappa = 0$, $\Gamma = 150$) and wave numbers $q = (1.45, 1.63, 2.17, 2.35)$, which are consistent with the box size and span a range that reveals the unusual behavior of the HK model. The parameter η_3 is obtained from the MD results using the least squares fitting method. The HK results exhibit two clear peaks in the low-wave-number regime; the right peak weakens as the wave number increases. The DSF obtained from the HK model gives better results when q is large.

All of the models examined in this work predict that the DSF exhibits a high-frequency tail (see Table I). Our MD results support the existence of this high-frequency tail, the form of which reveals that many sum rules are finite. Figures 9(a) and 9(b) show the DSF for moderate coupling [($\kappa = 1$, $\Gamma = 72$) and ($\kappa = 2$, $\Gamma = 158$)], and Figs. 9(c) and 9(d) show the asymptotic power of the DSF at the mid- to high-frequency limit for $\kappa = 0$ and $\kappa = 3$. In Figs. 9(a) and 9(b), we denote a portion of our MD results with square shapes to illustrate a spurious result, ω^{-2}, which arises from limitations in the numerical Fourier transforms. We verified that the DSF results obtained using other simulation tools (e.g., LAMMPS [46] and QUANTUM ESPRESSO [47]) also yield this spurious result, regardless of the plasma parameters. Careful control of Fourier-transform error allows us to extract the high-frequency tail at intermediate frequencies. To our knowledge, the tail has only been examined by Selchow *et al.* [48], who reported that the DSF has an asymptote of $\omega^{-7.5}$. The DSF from Donko *et al.* [45] also showed an asymptotic tail, but its properties were not examined. Here, in our more complete study, we see that the asymptotic power varies as a function of κ, Γ, and q. In general, the power varies between $-\infty$ and ~ -6, in disagreement with all of the theoretical

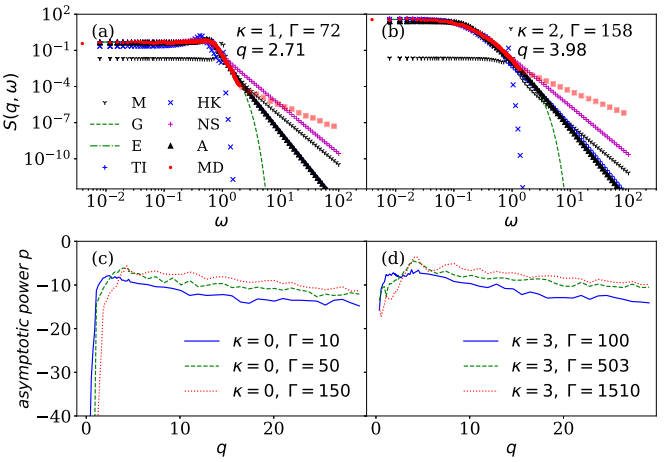

FIG. 9. The DSF from the seven theoretical models and our MD results for different parameter values (upper panels) and the asymptotic power of the DSF from the MD results at the mid- to high-frequency limit (lower panels). Panels (a) and (b) show the DSF with ($\kappa = 1$, $\Gamma = 72$) and ($\kappa = 2$, $\Gamma = 158$), respectively, and panels (c) and (d) show the asymptotic power of the DSF from the MD results at high frequency for $\kappa = 0$ and $\kappa = 3$, respectively. We denote a portion of our MD results in square shapes to indicate a spurious result, ω^{-2}, which arises from limitations when using numerical Fourier transforms. At intermediate frequencies, the power p is obtainable from MD simulations and varies from $p = -\infty$ to $p \sim -6$. Table I shows that none of the theoretical models can predict the asymptotic power variation seen in the MD simulation results.

models and indicating that only a small number of finite moments exist.

It is interesting to examine these results in the time domain, through the intermediate scattering function $F(q,t)$. Figure 10 shows the magnitude of $F(q,t)$ obtained from the DSF. In Fig. 10, we remove the spurious results caused by numerical Fourier transforms. Figure 10(a) shows that all models fail to predict the MD results. However, in Fig. 10(b), it is interesting

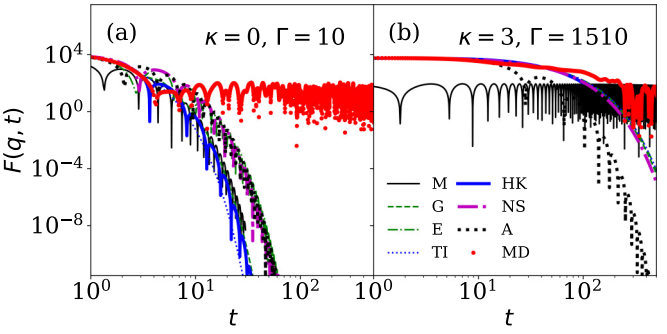

FIG. 10. Log-log plot of the intermediate scattering function (ISF) $F(q,t)$ calculated using several theoretical models and from our MD data for different plasma parameter values. Panel (a) shows the ISF at the lower boundary of the liquid regime ($\kappa = 0$, $\Gamma = 10$), and panel (b) shows the ISF near the upper boundary of the liquid regime ($\kappa = 3$, $\Gamma = 1510$). The wave number is set to $q = 5.6$ in both cases. Only the Mermin model shows fairly good agreement with the MD results (shown in red) at large t; all of the other models decay quickly.

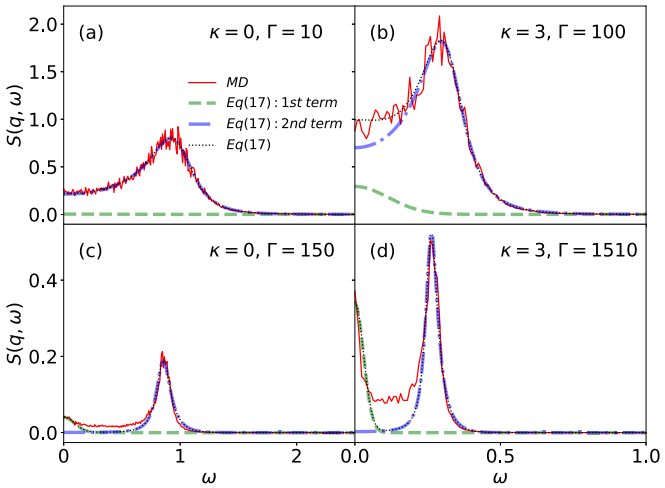

FIG. 11. A comparison of the DSF otained from the MD data and the fitting form for the DSF in (17). The MD DSF and the fitting form for the DSF are shown for moderate coupling regimes in panels (a) and (c) and for strong coupling regimes in panels (c) and (d); the wave number was set to $q = 1.99$ in all cases.

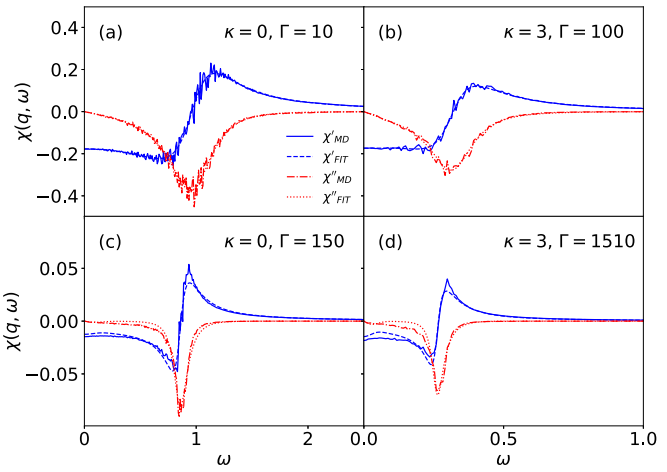

FIG. 12. The real and imaginary parts of $\chi(q, \omega)$ obtained from the MD and from the fitting form in (17). Panels (a) and (b) show moderate coupling regimes, and panels (c) and (d) show strong coupling regimes; the wave number was set to $q = 1.99$ in all cases. These results show that the fitting form in (17) gives good agreement with the MD results.

to note that only the M model shows fairly good agreement with the MD results at large t, despite its poor performance for the properties described above.

B. Fit of the DSF and the susceptibility

The plasmon-pole approximation is often used to provide a simple functional form for $S(q, \omega)$ based on sharp peaks (δ functions) that satisfy the basic sum rules [13]; however, examining Figs. 9(a) and 9(b) suggests the following fitting form, which includes finite peak widths and a power-law high-frequency tail:

$$S(q, \omega) = A_1 S_0(q, \omega) + \frac{A_2}{\left(\omega^2 - \omega_o^2\right)^{p/2} + \gamma(\omega^2)^{p_1/2}}, \quad p > p_1, \tag{17}$$

where $S_0(q, \omega)$ is the DSF of the ideal gas, p is the power-law exponent of the high-frequency tail, and A_1, A_2, γ, ω_o, and p_1 are fitting parameters; note that p here should not be confused with the p in the plasma frequency ω_p. The criterion $p > p_1$ should be satisfied to guarantee that the leading power at the high-frequency limit is p. Suitable initial guesses would be ω_o approximately equal to the peak frequency from the dispersion relation, $A_1 \sim S(q, 0)$, A_2 approximately equal to the peak amplitude of the dispersion relation, and γ approximately equal to the width of the dispersion relation. Figure 11 shows the DSF from the MD simulations, together with curve-fitting results using (17). Figures 11(a) and 11(b) show the MD DSF in two moderate coupling regimes, and Figs. 11(c) and 11(d) show the MD DSF in two strong coupling regimes. The wave number is $q = 1.99$ for all panels. In addition to the MD DSF curves, we plot the contribution to the DSF of each term of (17). The results show that coupling shifts the boundary between collective and random behavior to a lower value of the wave number q, and that the ideal-gas term plays an important role at very low frequencies when the screening or coupling is strong. While the MD DSF and the fit obtained using (17) differ around $\omega \sim 0.15$ in Figs. 11(c) and 11(d), overall, the fitting form in (17) gives good agreement with the MD results. However, close to the melting transition, intermediate frequencies in $S(q, \omega)$ are important and are not captured by our fitting form.

The susceptibility $\chi(q, \omega)$ represents an alternate representation of the linear response of the system and contains more information than the DSF through its real and imaginary parts. Figure 12 shows the susceptibility from the MD simulations and curve-fitting results. For the MD simulations, we use Eq. (16) to obtain the real and imaginary parts of the susceptibility. For the fitting form, we use Eq. (17) to obtain the DSF first, and then the fluctuation-dissipation theorem [Eq. (6)] to obtain the imaginary part of $\chi(q, \omega)$. Lastly, the Kramers-Kronig relations [Eqs. (13)] are used to obtain the real part of $\chi(q, \omega)$. Figures 12(a) and 12(b) show the susceptibility in moderate coupling regimes, and Figs. 12(c) and 12(d) show it in strong coupling regimes. The wave number is $q = 1.99$ for all panels. These results for the susceptibility also show that the fitting form in (17) gives good agreement with the MD results. Further investigation is needed to determine relations among the fitting parameters A_1, A_2, γ, ω_o, and p_1 via frequency moments of the DSF.

C. Double-plasmon peak

Figure 13 shows the DSF obtained from MD results for different plasma parameters and wave numbers. In Fig. 13(a), we can see that the DSF exhibits a second peak at $\omega = 2$, following a first peak at $\omega = 1$ for an OCP. This second peak is the double-plasmon resonance peak, as reported by Korolov *et al.* [49]. This peak is damped as the wave number increases. Figures 13(b)–13(d) show the DSF for YOCP cases. The double-plasmon peak amplitude is small and is increasingly damped as κ increases. In fact, for $\kappa = 2$ and 3, no double-plasmon peak is observed. In Figs. 13(a)–13(d), we select coupling parameters which are close to the lower liquid

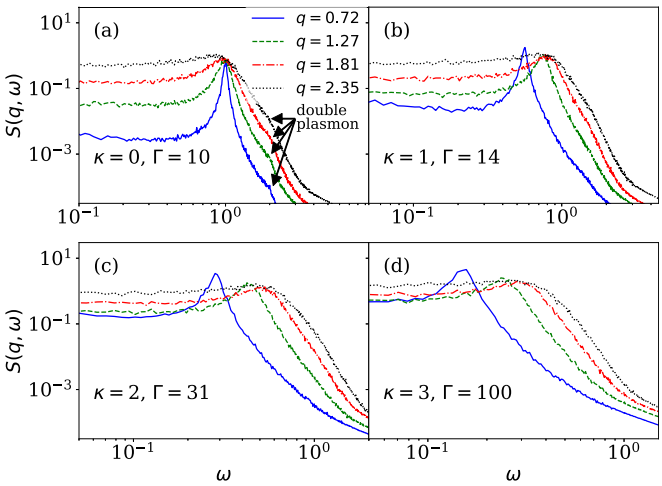

FIG. 13. The double-plasmon resonance peak in the DSF obtained from the MD results. The DSF is shown for several wave numbers for each of four different sets of plasma parameters. Panel (a) shows that the OCP exhibits the double-plasmon resonance peak at $\omega = 2$. The peak amplitude of the double-plasmon resonance peak decreases as the wave number increases. Panels (b) through (d) suggest that the relative strength of the double-plasmon resonance peak decreases (larger width and smaller peak) with larger κ.

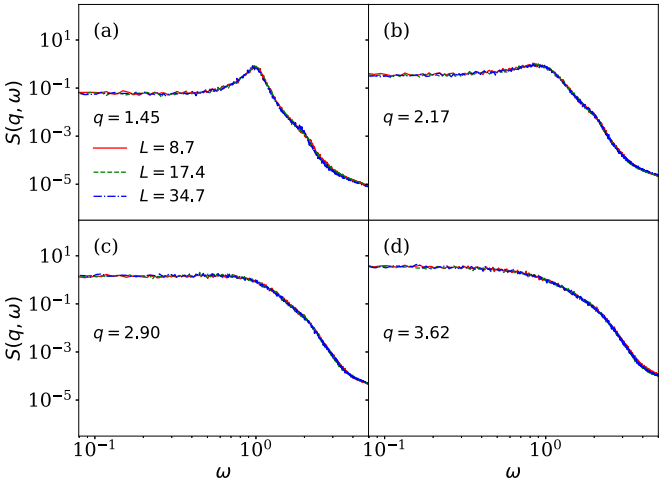

FIG. 14. The DSF calculated from MD data obtained using different simulation-box sizes. The plasma parameters are $\kappa = 0.1$ and $\Gamma = 10$. The properties of the second, double-plasmon resonance peak do not change with the size of the simulation box. The amplitude of the second peak decreases as the wave number increases, as expected.

boundary values in Fig. 1, and therefore, the effective coupling parameter is almost constant. The results in this figure suggest that this double-plasmon peak has a strong dependence on κ and weak dependence on q.

The sound speed of the OCP is infinite, and therefore, the second peak in Fig. 13(a) does not occur as an artifact of the PBC; to confirm this, we further investigated whether the double-plasmon peak is an artifact of the PBC for the YOCP. If the second peak occurs as a result of the PBC, then the peak location would depend on the size of the simulation box. Figure 14 shows the DSF calculated from MD data obtained using different box sizes. The plasma parameters ($\kappa = 0.1$, $\Gamma = 10$) were chosen for these simulations because, as we can see in Fig. 13, it is difficult to observe the second peak when $\kappa \geqslant 1$. In Fig. 14, we see that the properties of the second peak do not change with the size of the simulation box. The amplitude of the second peak decreases as the wave number increases, as expected. Therefore, we conclude that the double-plasmon peak is not an artifact of the size of the simulation box and is a real, physical phenomenon missed by all of the models.

VI. CONCLUSIONS

We have compared seven diverse theoretical models with highly accurate MD simulation results. These comparisons, which include dispersion relations, the intermediate scattering function $F(q, t)$, and the DSF $S(q, \omega)$, reveal that none of the models can predict these three quantities well even within a limited range of plasma parameters. The M model, which lacks correlation information and satisfies only the particle-conservation law, poorly predicts dispersion properties; this model is therefore limited to weakly coupled plasmas, where it adds little value [10,37]. The HK model satisfies the same three sum rules as most of the other models but exhibits a spurious second peak in the DSF at moderate to large q; further work is needed to understand this poor behavior. The TI, A, E, and G models all predict approximately the same dispersion, with a small error in A for the ion-acoustic wave.

Perhaps surprisingly, these theoretical models have very different high-frequency behaviors and thereby expose limitations to employing only the three basic sum rules. Moreover, in contrast with the high-frequency predictions of the sum-rule models, the MD results reveal that the DSF has an asymptotic power-law tail, with nontrivial dependencies on the plasma parameters κ and Γ, as well as the wave number q. This asymptotic power-law behavior severely limits extensions to the sum-rule approaches because there are a finite number of finite moments. This power law suggests a fitting form of the DSF which is accurate over a wide range of plasma parameters and wave numbers. In addition, we uncovered numerical issues in the course of this study; the computational Fourier transform gives a fictitious power -2 of ω in the high-frequency tail, which makes it challenging to directly obtain other dynamic properties, such as the response function and the DLFC.

The results of this work motivate further studies to extend the theoretical models examined here to include more information beyond three moments and a damping parameter, and to examine the sensitivity of the models in specific applications, such as stopping power [10] and XRTS at intermediate (q, ω).

All data can be found in Ref. [50].

ACKNOWLEDGMENT

This work was supported by the Air Force Office of Scientific Research under AFOSR Grant No. FA9550-17-1-0394.

[1] A. Diaw and M. S. Murillo, A dynamic density functional theory approach to diffusion in white dwarfs and neutron star envelopes, Astrophys. J. **829**, 16 (2016).

[2] W. J. Nellis, M. Ross, and N. C. Holmes, Temperature measurements of shock-compressed liquid hydrogen: Implications for the interior of Jupiter, Science **269**, 1249 (1995).

[3] J. H. Chu and L. I, Direct Observation of Coulomb Crystals and Liquids in Strongly Coupled rf Dusty Plasmas, Phys. Rev. Lett. **72**, 4009 (1994).

[4] T. C. Killian, Ultracold neutral plasmas, Science **316**, 705 (2007).

[5] O. A. Hurricane, D. A. Callahan, D. T. Casey, P. M. Celliers, C. Cerjan, E. L. Dewald, T. R. Dittrich, T. Döppner, D. E. Hinkel, L. F. Berzak Hopkins, J. L. Kline, S. Le Pape, T. Ma, A. G. MacPhee, J. L. Milovich, A. Pak, H.-S. Park, P. K. Patel, B. A. Remington, J. D. Salmonson, P. T. Springer, and R. Tommasini, Fuel gain exceeding unity in an inertially confined fusion implosion, Nature (London) **506**, 343 (2014).

[6] M. S. Murillo, Viscosity estimates of liquid metals and warm dense matter using the Yukawa reference system, High Energy Density Phys. **4**, 49 (2008).

[7] T. Komatsu, N. Yoshii, S. Miura, and S. Okazaki, A large-scale molecular dynamics study of dynamic structure factor and dispersion relation of acoustic mode in liquid and supercritical water, Fluid Phase Equilib. **226**, 345 (2004).

[8] J. Sarnthein, A. Pasquarello, and R. Car, Origin of the high-frequency doublet in the vibrational spectrum of vitreous SiO_2, Science **275**, 1925 (1997).

[9] W. Jin, P. Vashishta, R. K. Kalia, and J. P. Rino, Dynamic structure factor and vibrational properties of SiO_2 glass, Phys. Rev. B **48**, 9359 (1993).

[10] M. D. Barriga-Carrasco, Proton stopping using a full conserving dielectric function in plasmas at any degeneracy, Phys. Rev. E **82**, 046403 (2010).

[11] I. Nagy, J. László, and J. Giber, Dynamic local field correction in the calculation of electronic stopping power, Z. Phys. A: At. Nucl. **321**, 221 (1985).

[12] E. G. Brandt and O. Edholm, Dynamic structure factors from lipid membrane molecular dynamics simulations, Biophys. J. **96**, 1828 (2009).

[13] M. S. Murillo, X-ray Thomson scattering in warm dense matter at low frequencies, Phys. Rev. E **81**, 036403 (2010).

[14] S. Ichimaru, H. Iyetomi, and S. Tanaka, Statistical physics of dense plasmas: Thermodynamics, transport coefficients, and dynamic correlations, Phys. Rep. **149**, 91 (1987).

[15] J. P. Hansen, E. L. Pollock, and I. R. McDonald, Velocity Autocorrelation Function and Dynamical Structure Factor of the Classical One-Component Plasma, Phys. Rev. Lett. **32**, 277 (1974).

[16] J. P. Hansen, I. R. McDonald, and E. L. Pollock, Statistical mechanics of dense ionized matter. III. Dynamical properties of the classical one-component plasma, Phys. Rev. A **11**, 1025 (1975).

[17] S. Tanaka and S. Ichimaru, Dynamic theory of correlations in strongly coupled, classical one-component plasmas: Glass transition in the generalized viscoelastic formalism, Phys. Rev. A **35**, 4743 (1987).

[18] J. Hong and C. Kim, Dynamic structure of strongly coupled one-component plasmas, Phys. Rev. A **43**, 1965 (1991).

[19] S. V. Adamjan, T. Meyer, and I. M. Tkachenko, OCP dynamical structure factor and the plasma dispersion: Method of moments, Contrib. Plasma Phys. **29**, 373 (1989).

[20] Y. V. Arkhipov, A. Askaruly, D. Ballester, A. E. Davletov, I. M. Tkachenko, and G. Zwicknagel, Dynamic properties of one-component strongly coupled plasmas: The sum-rule approach, Phys. Rev. E **81**, 026402 (2010).

[21] Y. V. Arkhipov, A. B. Ashikbayeva, A. Askaruly, A. E. Davletov, and I. M. Tkachenko, Dielectric function of dense plasmas, their stopping power, and sum rules, Phys. Rev. E **90**, 053102 (2014).

[22] Y. V. Arkhipov, A. B. Ashikbayeva, A. Askaruly, A. E. Davletov, S. Syzganbaeva, A. E. Davletov, and I. M. Tkachenko, Dense plasma dynamic structure factor simulation data vs the method of moments, Contrib. Plasma Phys. **55**, 381 (2015).

[23] Y. V. Arkhipov, A. Askaruly, A. E. Davletov, D. Y. Dubovtsev, Z. Donko, P. Hartmann, I. Korolov, L. Conde, and I. M. Tkachenko, Direct Determination of Dynamic Properties of Coulomb and Yukawa Classical One-Component Plasmas, Phys. Rev. Lett. **119**, 045001 (2017).

[24] N. D. Mermin, Lindhard dielectric function in the relaxation-time approximation, Phys. Rev. B **1**, 2362 (1970).

[25] C. Fortmann, A. Wierling, and G. Röpke, Influence of local-field corrections on Thomson scattering in collision-dominated two-component plasmas, Phys. Rev. E **81**, 026405 (2010).

[26] J. P. Mithen, J. Daligault, and G. Gregori, Extent of validity of the hydrodynamic description of ions in dense plasmas, Phys. Rev. E **83**, 015401(R) (2011).

[27] J. Vorberger, Z. Donko, I. M. Tkachenko, and D. O. Gericke, Dynamic Ion Structure Factor of Warm Dense Matter, Phys. Rev. Lett. **109**, 225001 (2012).

[28] T. Dornheim, S. Groth, J. Vorberger, and M. Bonitz, *Ab initio* Path Integral Monte Carlo Results for the Dynamic Structure Factor of Correlated Electrons: From the Electron Liquid to Warm Dense Matter, Phys. Rev. Lett. **121**, 255001 (2018).

[29] Y. C. Chen, C. E. Simien, S. Laha, P. Gupta, Y. N. Martinez, P. G. Mickelson, S. B. Nagel, and T. C. Killian, Electron Screening and Kinetic-Energy Oscillations in a Strongly Coupled Plasma, Phys. Rev. Lett. **93**, 265003 (2004).

[30] U. Konopka, G. E. Morfill, and L. Ratke, Measurement of the Interaction Potential of Microspheres in the Sheath of a rf Discharge, Phys. Rev. Lett. **84**, 891 (2000).

[31] D. Gilles, F. Lambert, J. Clérouin, and G. Salin, Yukawa Monte Carlo and orbital free molecular dynamics approaches for the equation of state and structural properties of hot dense matter, High Energy Density Phys. **3**, 95 (2007), Radiative properties of hot dense matter (Special Issue).

[32] T. G. White, S. Richardson, B. J. B. Crowley, L. K. Pattison, J. W. O. Harris, and G. Gregori, Orbital-Free Density-Functional Theory Simulations of the Dynamic Structure Factor of Warm Dense Aluminum, Phys. Rev. Lett. **111**, 175002 (2013).

[33] M. S. Murillo, Ultrafast phase-space dynamics of ultracold, neutral plasmas, J. Phys. A: Math. Theor. **42**, 214054 (2009).

[34] D. S. Lemons, M. S. Murillo, W. Daughton, and D. Winske, Two-dimensional wake potentials in sub- and supersonic dusty plasmas, Phys. Plasmas **7**, 2306 (2000).

[35] H. Totsuji and H. Kakeya, Dynamical properties of two-dimensional classical electron liquids, Phys. Rev. A **22**, 1220 (1980).
[36] G. Dharuman, L. G. Stanton, J. N. Glosli, and M. S. Murillo, A generalized Ewald decomposition for screened Coulomb interactions, J. Chem. Phys. **146**, 024112 (2017).
[37] K. Morawetz and U. Fuhrmann, General response function for interacting quantum liquids, Phys. Rev. E **61**, 2272 (2000).
[38] K. S. Singwi, M. P. Tosi, R. H. Land, and A. Sjölander, Electron correlations at metallic densities, Phys. Rev. **176**, 589 (1968).
[39] P. Vashishta and K. S. Singwi, Electron correlations at metallic densities V, Phys. Rev. B **6**, 875 (1972).
[40] K. N. Pathak and P. Vashishta, Electron correlations and moment sum rules, Phys. Rev. B **7**, 3649 (1973).
[41] N. K. Ailawadi, A. Rahman, and R. Zwanzig, Generalized hydrodynamics and analysis of current correlation functions, Phys. Rev. A **4**, 1616 (1971).
[42] J. P. Boon and S. Yip, *Molecular Hydrodynamics*, 1st ed. (Dover, New York, 1991).
[43] W. Daughton, M. S. Murillo, and L. Thode, Empirical bridge function for strongly coupled Yukawa systems, Phys. Rev. E **61**, 2129 (2000).
[44] A. Savitzky and M. J. E. Golay, Smoothing and differentiation of data by simplified least squares procedures, Anal. Chem. **36**, 1627 (1964).
[45] Z. Donko, G. J. Kalman, and P. Hartmann, Dynamical correlations and collective excitations of Yukawa liquids, J. Phys.: Condens. Matter **20**, 413101 (2008).
[46] LAMMPS, https://lammps.sandia.gov.
[47] QUANTUM ESPRESSO, http://www.quantum-espresso.org.
[48] A. Selchow, G. Röpke, A. Wierling, H. Reinholz, T. Pschiwul, and G. Zwicknagel, Dynamic structure factor for a two-component model plasma, Phys. Rev. E **64**, 056410 (2001).
[49] I. Korolov, G. J. Kalman, L. Silvestri, and Z. Donko, The dynamical structure function of the one-component plasma revisited, Contrib. Plasma Phys. **55**, 421 (2015).
[50] M. S. Murillo, High-frequency response of classical strongly coupled plasmas (2019), https://github.com/MurilloGroupMSU/Dense-Plasma-Properties-Database/tree/master/database.